EUROPEAN ORGANIZATION FOR NUCLEAR RESEARCH

COMPARISON OF PHOTON AND HADRON INDUCED PRODUCTION
OF ρ^0 MESONS
IN THE ENERGY RANGE OF 65 TO 175 GEV

The OMEGA Photon Collaboration

R. J. Apsimon[5], M. Atkinson[3], M. Baake[1], L. S. Bagdasarian[7], D. Barberis[2],
T. J. Brodbeck[4], N. Brook[3], T. Charity[4], A. B. Clegg[4], P. Coyle[3], S. Danaher[6],
S. Danagulian[7], M. Davenport[2], B. Dickinson[3], B. Diekmann[1], A. Donnachie[3],
A. T. Doyle[3], J. Eades[2], R. J. Ellison[3], F. Fiedler[1], P. S. Flower[5], J. M. Foster[3],
W. Galbraith[6], P. I. Galumian[7], C. Gapp[1], F. Gebert[1], G. Hallewell[5], K. Heinloth[1],
R. C. W. Henderson[4], M. T. Hickman[4], K. C. Hoeger[1], R. P. Hofmann[1],
A. Holzkamp[1], S. Holzkamp[1], R. E. Hughes-Jones[3], M. Ibbotson[3], H. P. Jakob[1],
D. Joseph[1], N. R. Keemer[4], J. Kingler[1], G. Körsgen[1], S. D. Kolya[3], G. D. Lafferty[3],
H. McCann[3], R. McClatchey[2], C. McManus[3], D. Mercer[3], J. A. G. Morris[5],
J. V. Morris[5], D. Newton[4], A. O'Connor[4], R. Oedingen[1], A. G. Oganesian[7],
P. J. Ottewell[3], C. N. Paterson[5], E. Paul[1], D. Reid[3], H. Rotscheidt[1], P. H. Sharp[5],
S. Soeldner-Rembold[1], N. A. Thacker[6], L. Thompson[6], R. J. Thompson[3],
J. Waterhouse[3], A. S. Weigend[1], G. W. Wilson[4]

Abstract

The inclusive production of ρ^0 mesons was measured in γp and $h^\pm p$ collisions at beam energies of 65 GeV $\leq E_\gamma \leq$ 175 GeV and $E_h = 80, 140$ GeV, respectively, where h is π or K. Cross sections were determined for all beams and energies as functions of x_F (-0.1 $\leq x_F \leq$ 1.0), p_T ($0 \leq p_T \leq$ 3.5 GeV/c) and the polar decay angle of the ρ^0 by fitting the ρ^0 signal in $\pi^+\pi^-$ mass distributions. The ρ^0 line shape is found to be distorted from a pure Breit-Wigner distribution throughout most of the x_F- p_T plane for both photon and hadron beams and a simple explanation is suggested. Throughout the paper emphasis is put on the comparison of photon and hadron beam data. The comparison of cross sections of γp and hp data provides a measure of the Vector Meson Dominance factor throughout the x_F- p_T range of the ρ^0. The ρ^0 production at low p_T can be described for both photon and hadron beams by a triple regge model at large x_F. Similarly central production is well described by the quark-antiquark fusion model. At large p_T there is an excess of ρ^0 photoproduction which is consistent with the expected onset of pointlike photon interactions.

(Submitted to Z. Phys. C)

1) Physikalisches Institut, Universität, Nussallee 12, D-5300 Bonn, Federal Republic of Germany
2) CERN, CH-1211 Geneva 23, Switzerland
3) Department of Physics, The University, Manchester M13 9PL, England
4) School of Physics and Materials, Lancaster University, Lancaster LA1 4YB, England
5) Rutherford-Appleton Laboratory, Chilton, Didcot, Oxon OX11 0QX, England
6) Department of Physics, University of Sheffield, Sheffield S3 7RH, England
7) Yerevan Physics Institute, Markavion St. 2, SU-375 036 Yerevan, Armenia, USSR

1   INTRODUCTION

Measurements are reported of the reactions
$$\gamma p \to \rho^0 X; \quad 65 \text{ GeV} \leq E_\gamma \leq 175 \text{ GeV}$$
and
$$h^\pm p \to \rho^0 X; \quad E_h = 80 \text{ GeV and } 140 \text{ GeV, respectively}$$

where h is π or K and X ($\neq$ p) the hadronic systems produced together with the ρ^0 containing at least two charged tracks.

The reactions were measured with the OMEGA spectrometer at the CERN-SPS (experiment WA69). A total of $20 \cdot 10^6$ photon induced triggers and $24 \cdot 10^6$ hadron induced triggers were recorded. The latter consist of four parts according to beam energies and charge polarities ($4 \cdot 10^6$ each at ± 80 GeV and $8 \cdot 10^6$ each at ± 140 GeV). The ρ^0 signal was measured by fitting a resonance profile to inclusive $\pi^+\pi^-$ mass distributions as a function of three kinematical variables of the ρ^0: the Feynman variable $x_F = (p_L^{CMS})/(p_{max}^{CMS})$, the transverse momentum p_T with respect to the beam direction and the polar decay angle of the π^+ with respect to the ρ^0 momentum in the overall centre-of-mass system. Corresponding differential cross sections were obtained in the range of $-0.1 \leq x_F \leq 1$, $p_T \leq 3.5$ GeV and essentially for the whole decay angular range of the ρ^0. It is well known that the total cross section ratio between photo- and hadro-induced production of hadronic final states is of the order of $1/200$ and can be interpreted in terms of the Vector Meson Dominance Model (VMD) which assumes that the photon behaves like an appropriate mixture of vector meson states [1]. However until recently, little was known on whether this model is adequate to describe the ratio of cross sections in the x_F- p_T plane for inclusive particle production: first results were published on inclusive single charged particle production from this experiment [2], and are complemented by the results in this paper.

Here results on inclusive ρ^0 production are presented subdividing them in three parts with respect to three distinct kinematical areas in the x_F- p_T plane of the ρ^0:

1.   Large x_F ($x_F \geq 0.8$) – the triple–regge region, where the ρ^0 production is dominated by regge-exchange.

2.   Low p_T ($p_T \leq 1.6$ GeV/c) and low x_F ($-0.1 \leq x_F \leq 0.7$) – the "central region" with ρ^0 production described by the quark-antiquark fusion model where one quark or antiquark is picked up from the beam particle (VMD-photon or pion/kaon, respectively) and the other one from the target proton [3].

3.   Large p_T ($p_T \geq 1.6$ GeV/c) and all x_F – the region of "pointlike photon interactions" where the comparison between photon- and hadron-induced data indicates a relative excess of particles for the photon-induced data. This excess was already measured for inclusive π production [2, 4] and azimuthal energy flows [5] and is well in accord with QCD calculations for the lowest-order pointlike photon processes photon-gluon fusion and QCD-Compton.

2   THE EXPERIMENT

The data reported in this paper were taken at the CERN-Omega Spectrometer. The setup is shown in fig. 1. The photon beam was obtained as e^- bremsstrahlung from a tagging target. The single photon energy is determined by measuring the incoming and outgoing electron and covers the range 65 GeV $\leq E_\gamma \leq 175$ GeV. The hadron beams provided charged particles of both charges and two energies of 80 and 140 GeV. The
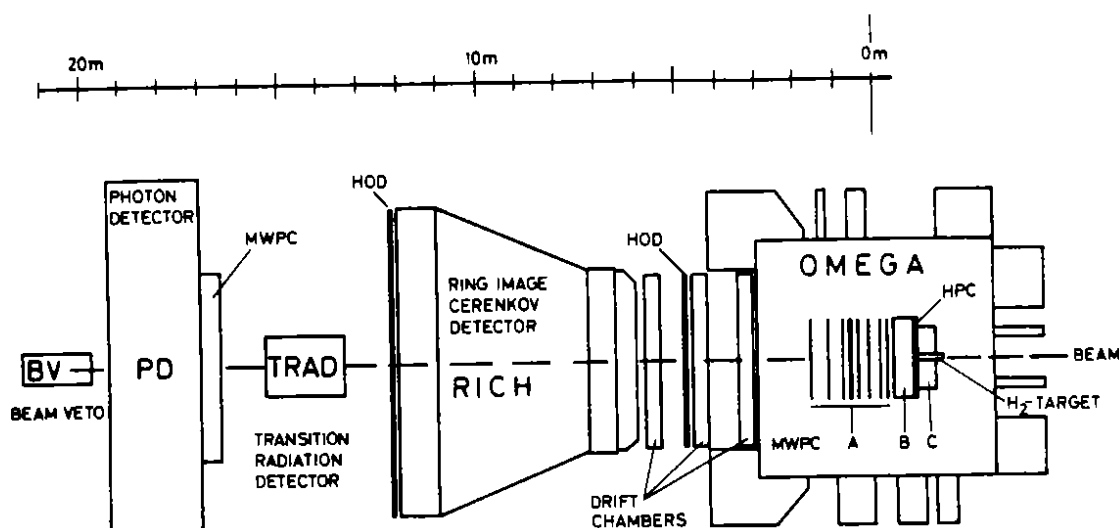
Figure 1: Schematic layout of the experiment

π/K ratio in this beam was measured and adjusted in the trigger by means of differential Cherenkov counters (CEDAR's) in the beamline. It was arranged to be 2:1 by accepting only 25% of the incoming π's. A system of MWPC's and DC's served to reconstruct charged secondaries, a ring image Cherenkov counter (RICH) and a transition radiation detector (TRAD) to identify $e^\pm$, $\pi^\pm$, $K^\pm$ and fast protons. A lead-liquid scintillator sandwich calorimeter (supplemented with a lead-fibre array around the beam hole) allowed for π^0, η detection. A more detailed description is given elsewhere [2].

The trigger was tuned to the highest obtainable degree of uniformity between photons and hadrons. The necessity of rejecting e^+e^- pairs in γp data defines the most stringent constraint on the trigger which thus demands

— a signal from the endcap counter behind the hydrogen target and no signal from a beam veto counter at the very end of the setup to reject events with energy measurement spoiled by double bremsstrahlung

— at least one track outside the median plane of the spectrometer (where the bulk of e^+e^- pairs is to be expected).

This track was defined by a correlated coincidence between two hodoscope arrays in front and at the rear of the ring image Cherenkov counter equipped with slits in the e^+e^- contaminated median plane. Moreover no electromagnetic signals were permitted from the photon calorimeter in a zone which matches with projections of the hodoscope slits.

The only differences for the two beam types were the requirements of

— a signal from a tagged beam electron in the γp data

— a signal from the CEDAR's in the hadron data.

For genuine hadronic final states these trigger requirements correspond to a rather weak restriction, so that for both beam types a trigger on σ^{tot} was effectively provided.

There was a significant contamination of electromagnetic pairs in the photon data. These were eliminated after pattern recognition by requiring at least 4 charged tracks from a vertex. In addition fiducial cuts on the vertex position and beam particle reconstruction were applied.
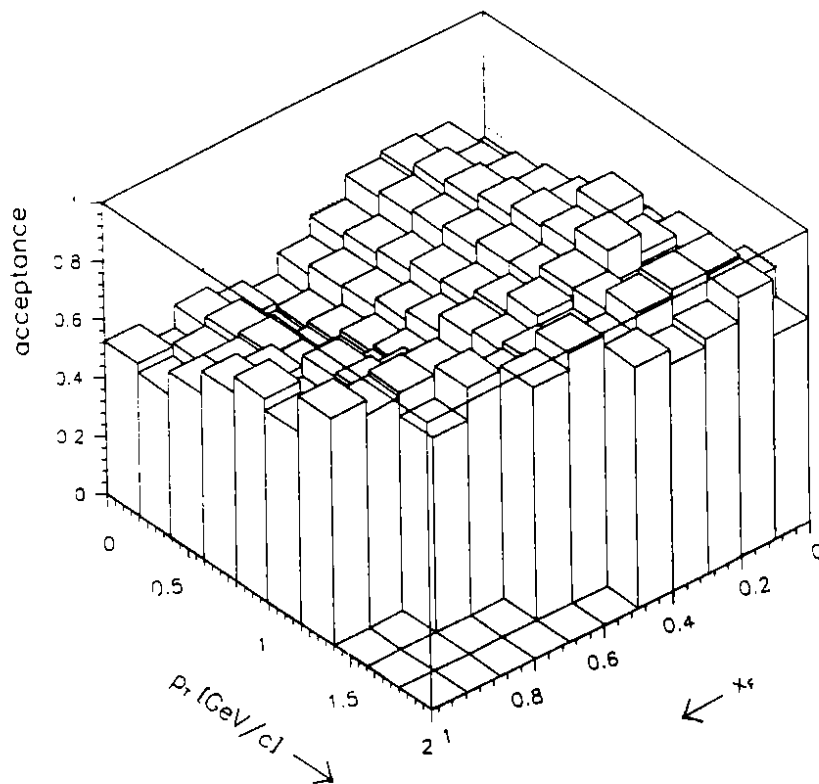
Figure 2: Acceptance of ρ^0 in $\gamma p \to \rho^0 X$ as a function of x_F and p_T, 65 GeV $\leq E_\gamma \leq$ 110 GeV

The particle identifying devices (RICH and TRAD) were not used in general in this analysis because of their restrictive influence on the overall acceptance over the x_F- p_T plane, in particular at low x_F or at high p_T. The amount of unidentified $K^\pm$ mesons, however, in particular those from $K^*(890)$ and their influence on the $\pi^+\pi^-$ mass distributions were quantified using these devices.

The acceptance was evaluated by processing simulated ρ^0-mesons through a full simulation of experimental setup, trigger (program OMFATHAC [6]), event reconstruction (program TRIDENT [7]) and data selection as specified above. The input event generators were HERWIG [8] and LULOPT/LUCVDM [9] for low p_T hadro and photoproduction and LUCIFER [9] optimized for high p_T pointlike photoproduction (the output was checked for consistency where overlapping). The output "data" were subjected to the identical fit procedure to be described below. The resulting acceptance was found to change smoothly with x_F and p_T (fig. 2). All experimental results considered in the following were corrected for this acceptance.

3   FIT PROCEDURE FOR EXTRACTION THE ρ^0 SIGNAL

The number of ρ^0-mesons was determined by fitting a resonance profile and a background shape to $\pi^+\pi^-$ mass distributions taking into account all charged particles of the hadronic multiparticle final states and assigning to them the π mass. The mass range covered by the fit was in general 320 MeV/c^2 $\leq$ m($\pi^+\pi^-$) $\leq$ 2 GeV/c^2 and in the low x_F low p_T region 500 MeV/c^2 $\leq$ m($\pi^+\pi^-$) $\leq$ 2 GeV/c^2.

The ρ^0 resonance profile was parametrized by

$$\rho^0(m) = \frac{m \cdot m_0 \cdot \Gamma(m)}{(m^2 - m_0^2)^2 + m_0^2 \cdot \Gamma^2(m)} \tag{1}$$

4

$$\Gamma(m) = \Gamma_0 \cdot \frac{2 \cdot \left(\frac{m^2 - 4 \cdot m_\pi^2}{m_0^2 - 4 \cdot m_\pi^2}\right)^{l + \frac{1}{2}}}{1 + \frac{m^2 - 4 \cdot m_\pi^2}{m_0^2 - 4 \cdot m_\pi^2}} \qquad (2)$$

where m_0, Γ_0 are the ρ^0 mass and width according to the PDG values (770 MeV/c^2 and 153 MeV/c^2) and spin l=1 [10].

As a second resonance profile in the fitted mass range, the f_2 was taken into account using the same formulae (1) and (2) with mass, width and spin of $m_0 = 1274$ MeV/c^2, $\Gamma_0 = 185$ MeV/c^2 and l=2 [10]. There was no need to include other resonances, in particular there is no evidence of $f_0(975)$ in these data.

Besides direct resonance production the $\pi^+\pi^-$ mass distribution is distorted by reflections from the production of ω and K*(890).

The $\pi^+\pi^-$ mass distribution from $\omega \to \pi^+\pi^-\pi^0$ decays appears as a broad bump at about 500 MeV/c^2 so it might produce structure in the background just below the ρ^0 mass. Since inclusive ω production over the full range of x_F and p_T cannot be measured in this experiment the $\pi^+\pi^-$ slope was parametrized as found from event generators from inclusive ω photoproduction (LUCVDM tuned to an x_F and p_T dependence of ($\gamma p \to \omega X$) as measured at lower energies [3]). The amount of ω's could not be predicted reliably and was determined together with other parameters (see below) in the fit. A variation of this parameter within the fit error limits does not affect the ρ^0 signal significantly anywhere in the x_F- p_T plane.

In the absence of particle identification, a K*(890) signal in the $K^\pm\pi^\mp$ mass spectrum yields a bump in the $\pi^+\pi^-$ mass distribution close to the ρ^0 nominal mass value. Since for acceptance reasons charged particle identification was not used for this study the bump from $K^* \to K\pi$ shows up in the $\pi^+\pi^-$ mass distribution. A comparison of $K^* \to K\pi$ to $\rho^0 \to \pi\pi$ found from $K^\pm\pi^\mp$ and $\pi^+\pi^-$ mass distributions in which π and K are identified by RICH and TRAD yielded a ratio as a function of x_F and p_T which was implemented in the fit function as a fixed parameter; the shape of the reflections was obtained by simulations.

Other reflections, in particular the $\pi^+\pi^-$ mass distributions from the $\rho^0(1600) \to 4\pi$ decay, were estimated to be too low in magnitude to distort the ρ^0 profile. Moreover, misidentified e^+e^- pairs in γp data are neither important for the shape of the $\pi^+\pi^-$ mass distribution nor for the $\rho^0 \to \pi^+\pi^-$ decay angular distributions (see sect. 5).

The non-resonant and combinatorial background below the signals of ρ^0, f_2 and reflections of ω and K*(890) was found to be parametrized with sufficient precision by an empirical ansatz combining an exponential including a cubic term multiplied with a cutoff function (see e. g. [11]):

$$BG(m) = (m - 2 \cdot m_\pi)^{p_2} \cdot \exp(-p_3 \cdot m - p_4 \cdot m^2 - p_5 \cdot m^3) \qquad (3)$$

where p_2 to p_5 are free parameters adjusted by the fitting procedure.

At this stage the fit function was built up as follows:

$$F(m) = p_1 \cdot BG(m) + p_6 \cdot \{\rho^0(m) + p_0 \cdot K^*(m) + p_7 \cdot \omega(m)\} + p_8 \cdot f_2(m) \qquad (4)$$

where p_1 to p_8 are free parameters in the fit whereas p_0 was set as described above.

With the ansatz (4) a large fraction of fits were very poor because the ρ^0 signal appeared to be shifted to a lower mass value. An example of this is demonstrated in fig. 3 which shows a $\pi^+\pi^-$ mass spectrum together with a fit curve (a) and the ρ^0 signal separately (b).

5

Inspired by elastic photoproduction of ρ^0, i.e. $\gamma p \to \rho^0 p$, where a similar shift towards lower mass was observed [12] and described successfully by interference effects [13, 14] the fit function (4) was extended by adding another term in order to account for interference between the amplitudes of ρ^0 and coherent (nonresonant) p-wave $\pi^+\pi^-$ pairs in the background [13]:

$$I(m) = \frac{m_0^2 - m^2}{m \cdot \Gamma(m)} \cdot \rho^0(m) \tag{5}$$

$$F_I(m) = p_1 \cdot BG(m) + p_6 \cdot \{\rho^0(m) + p_0 \cdot K^*(m) + p_7 \cdot \omega(m) + p_9 \cdot I(m)\} + p_8 \cdot f_2(m) \tag{6}$$

The relevance of such a contribution beyond the elastic domain was already measured by [15]. It was checked that an ansatz with a correlated background $F(m) \propto BG \cdot (1 + \rho^0)$ does not lead to a better description. In particular, the mass shift is not removed by this latter ansatz.

With $F_I(\mathrm{m})$ good fits were obtained in the whole kinematical range of the ρ^0 (see for example figs. 3c and d). A substantial interference term is required. Fig. 4 shows the magnitude of the interference parameter p_9 of equation (6) as a function of x_F and p_T for the high energy of γp and hp data. The variation with energy is found to be $\leq 20\%$, while the typical error on the fitted value of p_9 is 20%. Fig. 4 shows that such an effect is not only a diffractive phenomenon in ρ^0 photoproduction and is to a lesser extent also present in hadroproduction at low x_F and p_T.

The cross sections of inclusive ρ^0 production were determined using eq. (6) throughout this study. The fit yielded 670,000 photo-induced ρ^0s and 1,400,000 / 350,000 from π/K beams summed over energy and charge.

4   CROSS SECTIONS

Cross sections of inclusive ρ^0 production were determined for two data sets at "low and high energies":
-   "low energy" includes 65 GeV $\leq \mathrm{E}_\gamma \leq$ 110 GeV and E_h = 80 GeV,
-   "high energy" includes 110 GeV $\leq \mathrm{E}_\gamma \leq$ 175 GeV and E_h = 140 GeV,
where h denotes a mixture of $\pi^\pm$ and $K^\pm$ induced data yielding a strange to nonstrange ratio in the beam as is expected by VMD for the photon (i.e. π:K = 2:1).

The cross sections covered ρ^0s in the range $-0.1 \leq x_F \leq 1$ at all p_T (i.e. $0 \leq p_T \leq 3.5$ GeV/c) and essentially the full ρ^0 decay angular range.

Tables 1 to 4 contain the cross sections $d^2\sigma/dx_F dp_T$ separately for γp and hp data at low and high energy, calculated for bins of 0.1 in x_F and 0.2 GeV/c in p_T.

The double differential cross sections in tables 1 to 4 are also displayed in fig. 5. Both γp and hp data show besides a pronounced peak in the central region (at low x_F and low p_T) another enhancement at high x_F and low p_T.

The errors in tables 1 to 4 are statistical ones resulting from the fit procedure. In addition there is a systematic uncertainty of the order of 15% in the overall normalisation of the cross sections.

Differential cross sections $d\sigma/dx_F$ and $d\sigma/dp_T$ were also determined for $\pi^\pm p$ and $K^\pm p$ data separately. They are shown in tables 5 and 6. They are consistent with the corresponding sums over rows and columns in tables 1 to 4.

Integrated cross sections in the range $-0.1 \leq x_F \leq 1$ for γp, πp and $K p$ at low and high energy determined with fits to the total $\pi^+\pi^-$ mass distributions are collected in table 7.
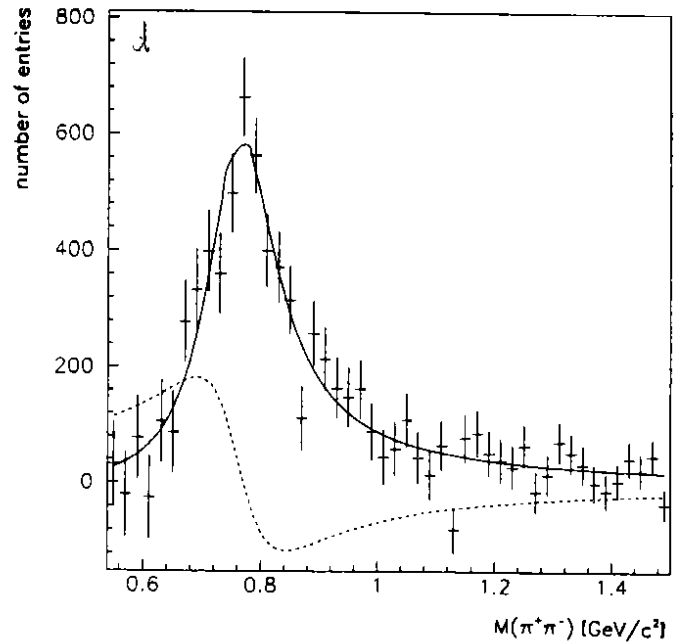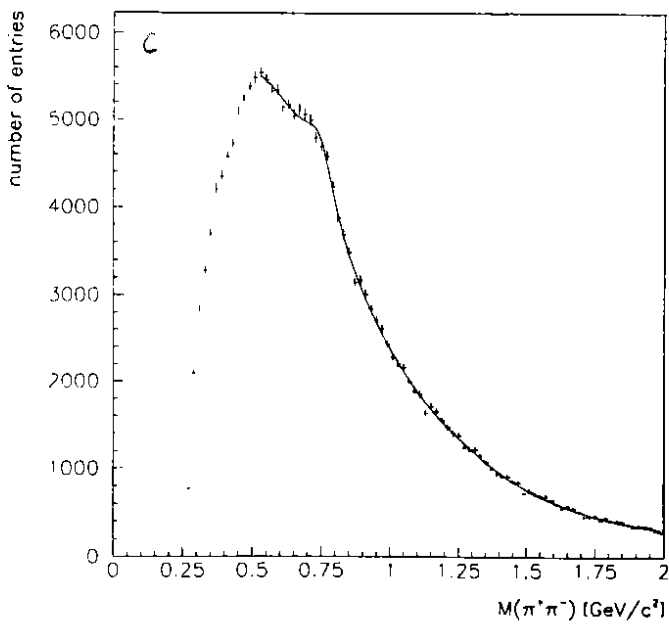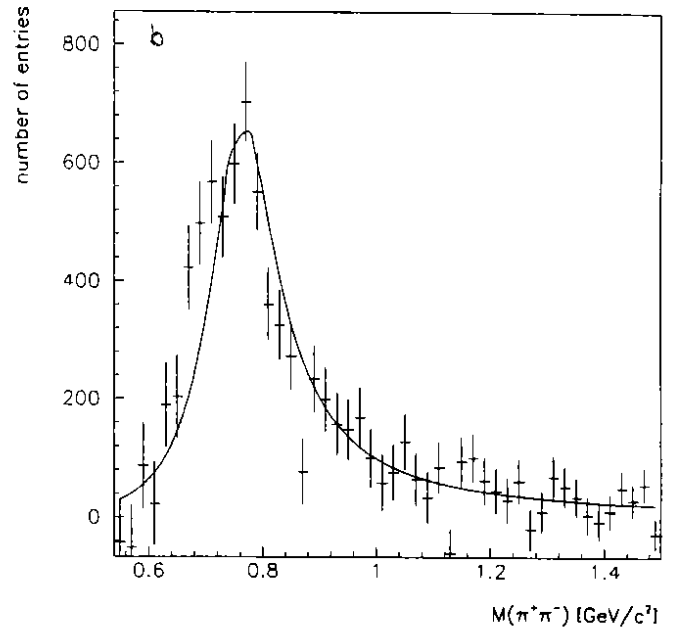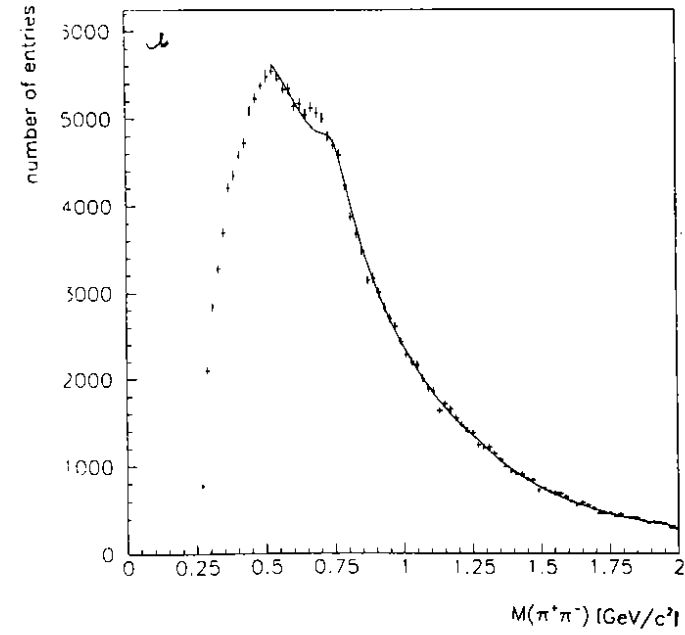
Figure 3: (a) $M(\pi^+\pi^-)$ distributions of photoproduced $\pi^+\pi^-$ pairs in the range $0.2 \leq x_F \leq 0.3$, $p_T \leq 0.2$ GeV/c (low energy data). The curve corresponds to the eq. (4). (b) ρ^0 signal and resonance curve according to (a). (c) The same data as in (a) but with the fit curve corresponding to eq. (6). (d) ρ^0 signal and resonance curve (solid line) according to (c). The dashed curve shows the interference term found in the fit.
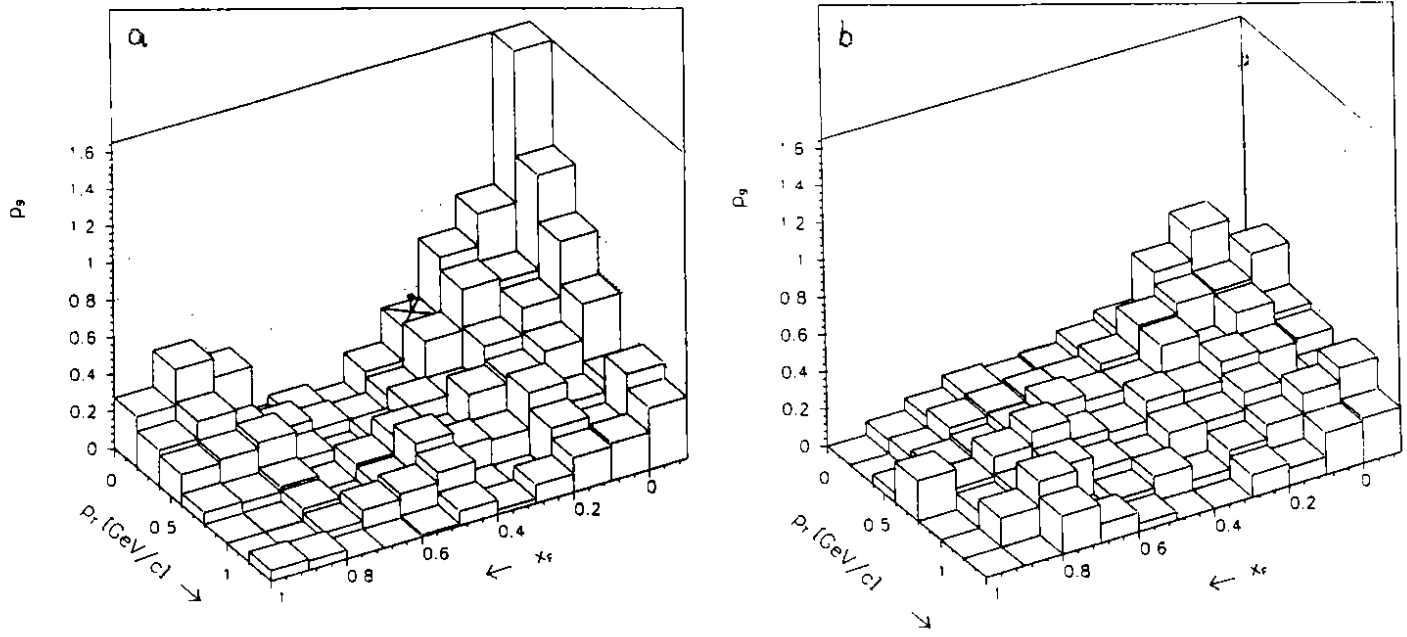
Figure 4: The strength of the interference term (parameter p_9, see text) determined by the fits according to eq. (6) as a function of x_F and p_T. (a) γp data, high energies. The bin indicated by the X corresponds to the data set in fig. 3: $p_9 = 0.38\pm0.08$; (b) hp data, high energy.

$x_F \longrightarrow$

$\longleftarrow \ p_T$ [GeV/c]

p_T / x_F	-0.1	0.0	0.1	0.2	0.3	0.4	0.5	0.6	0.7	0.8	0.9
0.0	10.33 ±2.88	12.15 ±4.16	17.33 ±1.76	15.04 ±1.02	13.19 ±0.95	10.21 ±0.68	7.63 ±0.54	4.55 ±0.52	3.93 ±0.34	5.15 ±0.28	11.47 ±0.33
0.2	21.63 ±2.69	34.52 ±2.17	35.82 ±2.57	27.99 ±1.27	21.39 ±1.05	18.09 ±1.60	11.55 ±0.62	10.43 ±0.59	9.62 ±0.49	11.50 ±0.37	29.99 ±0.45
0.4	33.23 ±2.41	35.83 ±2.52	30.96 ±2.01	27.97 ±1.37	20.36 ±0.94	18.19 ±0.85	15.10 ±0.74	12.69 ±1.36	8.02 ±0.31	10.51 ±0.33	19.75 ±0.37
0.6	16.48 ±2.15	24.38 ±1.96	24.50 ±1.36	18.33 ±2.51	15.12 ±0.73	12.68 ±0.72	11.52 ±0.62	8.14 ±0.22	5.75 ±0.26	5.71 ±0.22	7.15 ±0.28
0.8	10.46 ±1.11	13.08 ±1.20	10.14 ±0.95	9.53 ±0.63	8.73 ±0.56	7.23 ±0.49	5.36 ±1.22	4.08 ±0.36	2.99 ±0.19	2.46 ±0.17	2.47 ±0.12
1.0	5.60 ±0.71	7.59 ±0.84	4.47 ±0.43	4.35 ±0.45	3.78 ±0.35	3.49 ±0.32	2.78 ±0.25	2.35 ±0.23	1.64 ±0.13	1.29 ±0.08	1.13 ±0.09
1.2	2.66 ±0.41	2.47 ±0.40	3.07 ±0.33	2.28 ±0.29	1.86 ±0.39	1.72 ±0.22	1.23 ±0.15	0.72 ±0.13	0.78 ±0.08	0.69 ±0.05	0.34 ±0.04
1.4	0.70 ±0.31	1.04 ±0.22	1.41 ±0.30	1.13 ±0.19	0.94 ±0.14	0.73 ±0.13	0.45 ±0.11	0.40 ±0.09	0.34 ±0.07		
1.6	0.42 ±0.17	0.56 ±0.19	0.53 ±0.11	0.44 ±0.18	0.47 ±0.07	0.20 ±0.09	0.31 ±0.08				
1.8	0.23 ±0.07	0.35 ±0.09	0.32 ±0.08	0.21 ±0.08	0.15 ±0.06						

Table 1: $\mathrm{d}^2\sigma/dx_F dp_T(\gamma p \rightarrow \rho^0 X)$ in μb/(GeV/c), 65 GeV$\leq E_\gamma \leq$ 110 GeV

p_T [GeV/c] \ x_F	-0.1	0.0	0.1	0.2	0.3	0.4	0.5	0.6	0.7	0.8	0.9
0.0	7.04 ±1.91	15.82 ±2.56	19.11 ±2.02	15.89 ±1.27	12.04 ±1.02	10.56 ±1.00	7.41 ±0.95	5.12 ±0.52	4.32 ±0.43	8.14 ±0.21	14.74 ±0.52
0.2	32.54 ±3.84	50.40 ±3.97	36.40 ±2.51	33.08 ±2.16	24.24 ±1.27	19.14 ±1.06	13.78 ±1.03	10.87 ±0.71	9.21 ±0.52	11.36 ±0.48	34.95 ±0.40
0.4	36.74 ±6.31	52.70 ±3.30	34.21 ±2.23	30.27 ±1.58	23.59 ±1.93	17.71 ±1.03	13.56 ±0.94	9.46 ±0.74	7.99 ±0.44	9.22 ±0.37	20.13 ±0.48
0.6	25.70 ±2.66	31.21 ±2.21	25.26 ±1.59	17.39 ±1.31	16.48 ±0.98	11.04 ±0.81	8.17 ±0.58	7.33 ±0.72	5.51 ±0.31	5.44 ±0.27	7.77 ±0.45
0.8	16.19 ±1.39	17.63 ±1.52	10.83 ±1.13	9.54 ±0.67	9.45 ±0.69	6.93 ±0.54	5.45 ±0.52	4.07 ±0.40	2.63 ±0.31	3.31 ±0.20	2.78 ±0.14
1.0	7.64 ±1.04	7.70 ±0.46	7.01 ±0.62	5.11 ±0.50	3.11 ±0.55	3.04 ±0.38	3.45 ±0.31	1.76 ±0.29	1.48 ±0.13	1.27 ±0.14	1.31 ±0.08
1.2	3.36 ±0.59	4.11 ±0.46	2.70 ±0.43	2.46 ±0.36	1.84 ±0.32	1.09 ±0.25	1.18 ±0.21	0.89 ±0.12	0.68 ±0.09	0.56 ±0.07	0.49 ±0.05
1.4	1.78 ±0.34	1.53 ±0.31	1.18 ±0.27	1.08 ±0.25	1.07 ±0.13	0.63 ±0.15	0.57 ±0.10	0.39 ±0.08	0.31 ±0.07		
1.6	0.92 ±0.21	0.81 ±0.17	0.53 ±0.16	0.74 ±0.18	0.49 ±0.15	0.17 ±0.07	0.32 ±0.08				
1.8	0.32 ±0.13	0.54 ±0.11	0.56 ±0.11	0.36 ±0.10	0.14 ±0.14						

Table 2: $d^2\sigma/dx_F dp_T(\gamma p \to \rho^0 X)$ in μb/(GeV/c), 110 GeV$\leq E_\gamma \leq$ 175 GeV

p_T [GeV/c] \ x_F	-0.1	0.0	0.1	0.2	0.3	0.4	0.5	0.6	0.7	0.8	0.9
0.0	2.64 ±0.37	4.19 ±0.42	3.23 ±0.28	2.82 ±0.22	2.16 ±0.12	2.35 ±0.17	2.21 ±0.10	2.27 ±0.09	2.81 ±0.07	3.28 ±0.08	2.01 ±0.08
0.2	6.94 ±1.02	7.22 ±0.40	6.58 ±0.37	4.92 ±0.26	3.60 ±0.13	3.03 ±0.15	2.44 ±0.09	2.37 ±0.09	2.17 ±0.07	1.74 ±0.22	0.81 ±0.03
0.4	6.48 ±0.44	6.86 ±0.53	6.53 ±0.35	3.86 ±0.23	3.56 ±0.15	3.00 ±0.12	2.33 ±0.11	1.79 ±0.08	1.17 ±0.05	0.94 ±0.04	0.31 ±0.02
0.6	4.04 ±0.33	4.36 ±0.78	3.85 ±0.25	2.70 ±0.19	2.35 ±0.12	1.89 ±0.10	1.62 ±0.09	1.17 ±0.06	0.72 ±0.04	0.38 ±0.02	0.15 ±0.02
0.8	2.39 ±0.22	2.22 ±0.21	1.59 ±0.16	1.58 ±0.14	1.08 ±0.10	1.04 ±0.08	0.80 ±0.06	0.53 ±0.04	0.31 ±0.03	0.17 ±0.02	0.06 ±0.01
1.0	0.82 ±0.12	1.27 ±0.11	0.98 ±0.09	0.77 ±0.12	0.55 ±0.06	0.37 ±0.05	0.32 ±0.03	0.18 ±0.03	0.10 ±0.01	0.08 ±0.01	0.03 ±0.00
1.2	0.35 ±0.09	0.48 ±0.05	0.40 ±0.06	0.38 ±0.05	0.22 ±0.04	0.15 ±0.03	0.10 ±0.02	0.10 ±0.02	0.05 ±0.01	0.02 ±0.02	0.00 ±0.00
1.4	0.21 ±0.04	0.21 ±0.03	0.16 ±0.05	0.13 ±0.03	0.12 ±0.03	0.10 ±0.02	0.06 ±0.01	0.02 ±0.01	0.02 ±0.00		
1.6	0.07 ±0.02	0.05 ±0.01	0.10 ±0.02	0.05 ±0.01	0.05 ±0.01	0.02 ±0.01	0.02 ±0.01				
1.8	0.03 ±0.01	0.01 ±0.01	0.03 ±0.01	0.00 ±0.00	0.00 ±0.00						

Table 3: $d^2\sigma/dx_F dp_T(hp \to \rho^0 X)$ in mb/(GeV/c), $E_h =$ 80GeV

$x_F \rightarrow$

p_T [GeV/c] ↓

p_T \ x_F	-0.1	0.0	0.1	0.2	0.3	0.4	0.5	0.6	0.7	0.8	0.9
0.0	3.46 ±0.32	5.06 ±0.37	4.46 ±0.26	3.36 ±0.14	3.18 ±0.14	2.50 ±0.11	2.74 ±0.09	2.91 ±0.07	3.42 ±0.06	4.69 ±0.07	4.29 ±0.07
0.2	7.81 ±0.44	10.57 ±0.43	7.85 ±0.28	5.61 ±0.18	5.04 ±0.21	3.35 ±0.10	2.97 ±0.08	2.79 ±0.06	2.37 ±0.05	2.29 ±0.04	1.24 ±0.03
0.4	8.57 ±0.89	9.07 ±0.33	7.51 ±0.24	4.94 ±0.18	4.41 ±0.12	3.12 ±0.10	2.36 ±0.09	2.01 ±0.06	1.63 ±0.04	1.19 ±0.04	0.54 ±0.02
0.6	5.69 ±0.24	6.28 ±0.24	4.31 ±0.18	2.86 ±0.13	2.73 ±0.10	2.17 ±0.10	1.65 ±0.08	1.32 ±0.05	0.91 ±0.04	0.59 ±0.03	0.22 ±0.02
0.8	2.48 ±0.15	3.24 ±0.23	2.08 ±0.12	1.81 ±0.10	1.38 ±0.07	1.08 ±0.06	0.85 ±0.06	0.59 ±0.04	0.39 ±0.02	0.27 ±0.02	0.07 ±0.01
1.0	1.42 ±0.01	1.40 ±0.06	1.13 ±1.08	0.91 ±0.06	0.63 ±0.05	0.44 ±0.04	0.42 ±0.03	0.29 ±0.02	0.13 ±0.03	0.09 ±0.01	0.04 ±0.01
1.2	0.62 ±0.05	0.83 ±0.05	0.55 ±0.05	0.40 ±0.03	0.31 ±0.03	0.24 ±0.02	0.17 ±0.02	0.12 ±0.01	0.07 ±0.01	0.03 ±0.01	0.02 ±0.00
1.4	0.32 ±0.03	0.33 ±0.04	0.35 ±0.03	0.20 ±0.03	0.16 ±0.02	0.06 ±0.02	0.05 ±0.01	0.05 ±0.01	0.02 ±0.01		
1.6	0.12 ±0.02	0.11 ±0.02	0.11 ±0.01	0.11 ±0.01	0.06 ±0.02	0.03 ±0.01	0.04 ±0.01				
1.8	0.06 ±0.02	0.06 ±0.01	0.06 ±0.01	0.03 ±0.01	0.04 ±0.01						

Table 4: $d^2\sigma/dx_F dp_T(hp \rightarrow \rho^0 X)$ in mb/(GeV/c), $E_h = 140$GeV

$x_F \rightarrow$

		-0.1	0.0	0.1	0.2	0.3	0.4	0.5	0.6	0.7	0.8	0.9
γp 60-110GeV	[μb]	20.33 ±0.91	27.25 ±0.80	25.00 ±0.51	20.64 ±0.68	16.65 ±0.38	12.40 ±0.29	8.91 ±0.22	7.00 ±0.18	6.06 ±0.15	7.18 ±0.13	13.46 ±0.13
γp 110-175GeV	[μb]	26.21 ±0.61	37.41 ±1.19	28.14 ±0.85	19.51 ±1.56	15.16 ±0.44	10.45 ±0.30	7.06 ±0.23	5.77 ±0.18	5.35 ±0.15	6.99 ±0.14	14.37 ±0.16
πp 80GeV	[mb]	5.14 ±0.34	5.19 ±0.15	5.52 ±0.29	4.25 ±0.11	3.40 ±0.08	2.59 ±0.09	2.14 ±0.05	1.83 ±0.04	1.71 ±0.03	1.62 ±0.03	0.88 ±0.02
πp 140GeV	[mb]	6.20 ±0.19	8.52 ±0.23	6.17 ±0.16	4.15 ±0.23	3.68 ±0.12	2.51 ±0.07	1.90 ±0.04	1.75 ±0.04	1.68 ±0.03	1.76 ±0.03	1.39 ±0.02
Kp 80GeV	[mb]	3.77 ±1.25	4.39 ±0.70	2.25 ±0.66	1.86 ±0.58	1.28 ±0.03	1.03 ±0.74	0.44 ±0.11	0.25 ±0.08	0.14 ±0.03	0.00 ±0.00	0.00 ±0.00
Kp 140GeV	[mb]	4.56 ±0.55	5.30 ±0.59	3.74 ±0.29	2.34 ±0.10	1.76 ±0.06	1.01 ±0.05	0.65 ±0.02	0.38 ±0.02	0.26 ±0.01	0.19 ±0.00	0.11 ±0.00

Table 5: $d\sigma/dx_F(\gamma/hp \rightarrow \rho^0 X)$ in μb for γp data and in mb for πp and Kp data

p_T [GeV/c]	γp 65-110 GeV [nb/GeV]		γp 110-175 GeV [nb/GeV]		πp 80 GeV [μb/GeV]		πp 140 GeV [μb/GeV]		Kp 80 GeV [μb/GeV]		Kp 140 GeV [μb/GeV]	
0.0–0.2	9940.5 ±	356.1	9161.1 ±	302.7	2807.6 ±	127.3	3101.1 ±	109.2	1057.4 ±	346.6	965.7 ±	194.0
0.2–0.4	20223.7 ±	494.2	21071.5 ±	553.2	4764.5 ±	173.4	4638.7 ±	121.8	1889.1 ±	336.2	2512.7 ±	210.6
0.4–0.6	20021.6 ±	449.1	20597.7 ±	532.2	3796.6 ±	146.0	4531.8 ±	151.2	1703.3 ±	299.4	2154.3 ±	275.0
0.6–0.8	12957.3 ±	332.7	13319.9 ±	391.6	2396.8 ±	118.4	2683.1 ±	116.9	1237.3 ±	186.9	1464.5 ±	141.8
0.8–1.0	6455.9 ±	270.8	7171.1 ±	260.5	1210.2 ±	73.2	1480.8 ±	58.9	632.7 ±	152.0	755.7 ±	151.4
1.0–1.2	3491.7 ±	131.7	3968.1 ±	169.2	702.4 ±	40.1	704.5 ±	23.6	190.2 ±	29.1	499.4 ±	54.0
1.2–1.4	1651.2 ±	82.3	1723.3 ±	97.0	215.9 ±	19.4	318.2 ±	304.6	107.3 ±	103.2	287.2 ±	25.7
1.4–1.6	719.3 ±	51.9	797.9 ±	57.0	97.6 ±	11.7	143.4 ±	12.3	75.1 ±	13.7	98.4 ±	17.6
1.6–1.8	332.6 ±	32.4	421.5 ±	35.6	49.9 ±	6.5	66.0 ±	7.0	48.0 ±	14.1	49.3 ±	10.9
1.8–2.0	173.0 ±	17.1	207.6 ±	23.8	8.4 ±	7.2	26.4 ±	6.4	9.1 ±	9.5	31.3 ±	9.0
2.0–2.3	59.1 ±	9.1	68.3 ±	13.6	8.3 ±	7.8	11.2 ±	3.6	7.0 ±	3.5	16.4 ±	2.9
2.3–2.6	16.8 ±	2.9	28.2 ±	5.9	2.5 ±	1.2	3.3 ±	1.0	1.3 ±	1.2	4.6 ±	1.5
2.6–3.0	1.9 ±	1.8	5.1 ±	3.0	0.0 ±	0.0	0.4 ±	0.2	0.0 ±	0.0	1.0 ±	0.7
3.0–3.5	0.1 ±	0.1	3.4 ±	3.4	0.3 ±	0.2	0.2 ±	0.2	0.9 ±	0.6	0.0 ±	0.1

Table 6: $d\sigma/dp_T(\gamma/hp \to \rho^0 X)$ in nb/(GeV/c) for γp data and in μb/(GeV/c) for πp and Kp data, $-0.1 \leq x_F \leq 0.8$

γp ; 65-110 GeV	$(16.41 \pm 0.16)\mu$b
γp ;110-175 GeV	$(18.00 \pm 0.23)\mu$b
π^+p ; 80 GeV	(4.17 ± 0.06) mb
π^-p ; 80 GeV	(3.35 ± 0.05) mb
K^+p ; 80 GeV	(1.86 ± 0.10) mb
K^-p ; 80 GeV	(1.76 ± 0.09) mb
π^+p ;140 GeV	(4.62 ± 0.05) mb
π^-p ;140 GeV	(4.03 ± 0.05) mb
K^+p ;140 GeV	(2.35 ± 0.06) mb
K^-p ;140 GeV	(2.08 ± 0.07) mb

Table 7: Integrated cross sections $\sigma(\gamma/h\,p \to \rho^0 X)$ for different beams in the range $-0.1 \leq x_F \leq 1.0$, $p_T \leq 3.5$ GeV/c

Compared to previous measurements [16, 17, 18, 19, 20] the hadron induced ρ^0 cross sections reported above are lower by almost a factor of two. The requirement in this experiment for at least two additional charged particles corresponds to a restriction compared to the whole inelastic ρ^0 cross section. There are also substantial effects due to the method of analysis; the inclusion of a cubic term in the exponential of the function describing the background and the inclusion of the Söding type contribution both reduce the ρ^0 cross sections compared to previous analyses. There is no evidence for any discrepancy in the absolute normalisation between this and other experiments.

The arbitrarily normalized ρ^0 polar decay angular distribution $W(\cos\theta)$, where θ was measured in the s-channel helicity system, has been obtained by fits to the $\pi^+\pi^-$ mass distributions for 10 bins of $\cos\theta$. Two data sets were fitted which cover two ranges in x_F: $-0.1 \leq x_F \leq 0.5$ and $x_F \geq 0.8$. The data at low and high energies were added for the fits in order to improve statistics. The results are shown in fig. 6 for the γp data and in fig. 7 for the h$^\pm$p data. One notices pronounced differences between low and high x_F as well as between γp and hp data. The curve in fig. 6b corresponds to $W(\cos\theta) \propto (a + \sin^2\theta)$, with $a = 0.140 \pm 0.019$; $\sin^2\theta$ is the well known prediction for diffractive vector meson production with photons, while the additional background is due to other production mechanisms. The curve in fig. 7b is given by $W(\cos\theta) \propto (a + \cos^2\theta)$, with $a = 0.254 \pm 0.011$ (determined by the fit). Interpretations are discussed in sect. 5.3.

5   DISCUSSION

5.1   Distortion of the ρ^0 Line Shape

In diffractive ρ^0 photoproduction i.e. the reaction γp$\rightarrow \rho^0$p, the distortion of the ρ^0 line shape is well quantified by the Söding model [13, 14] which explains the phenomenon in terms of an interference between direct ρ^0 production and the production of nonresonant pion pairs. The latter arise from direct conversion of the photon, with subsequent diffractive scattering of the pions from the target. The ρ^0 line shape in diffractive photoproduction varies both with the incident photon energy and with the transverse momentum of the ρ, both variations being well described by the model. It is clear that precisely the same explanation can be applied to inclusive ρ^0 photoproduction at large x_F which is described by the triple regge exchange mechanism, discussed in section 5.3 below. We suggest that a similar mechanism operates over the whole of the x_F-p_T plane. In general, particle production is described by string fragmentation, and this can be directly into pions or into excited states such as the ρ^0. Some fraction of the direct pion production will generate pairs in a p-wave state which can then interfere with the direct ρ^0 production producing a distortion of the line-shape. It is not possible to quantify this explicitly, but there are two observations which support this hypothesis. The first is that the distortion of the ρ^0 line shape is greatest where the background under the ρ^0 is greatest. The second is that there is no distortion of the ρ line shape at high x_F, low p_T in the reaction $\pi^\pm$p$\rightarrow \rho^0$X as the analogue of the Söding model cannot exist.

5.2   Vector Meson Dominance

In fig. 8 the ratio of cross sections for γp and hp data is shown as a function of x_F and p_T of the ρ^0. It was calculated from the cross sections in tables 1 to 4; data of low and high energy were combined.

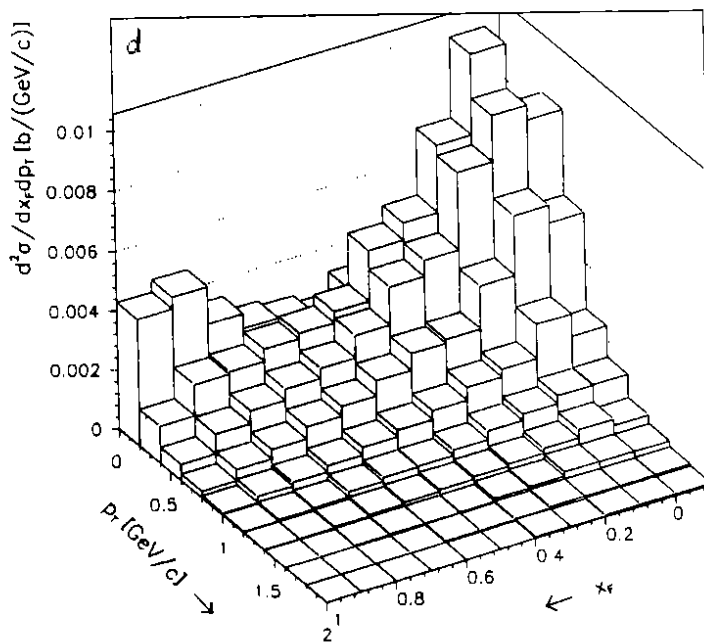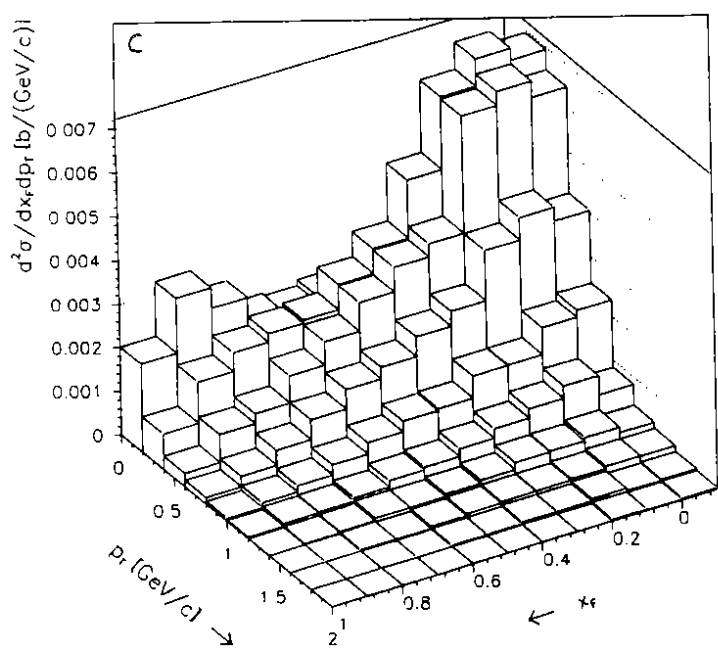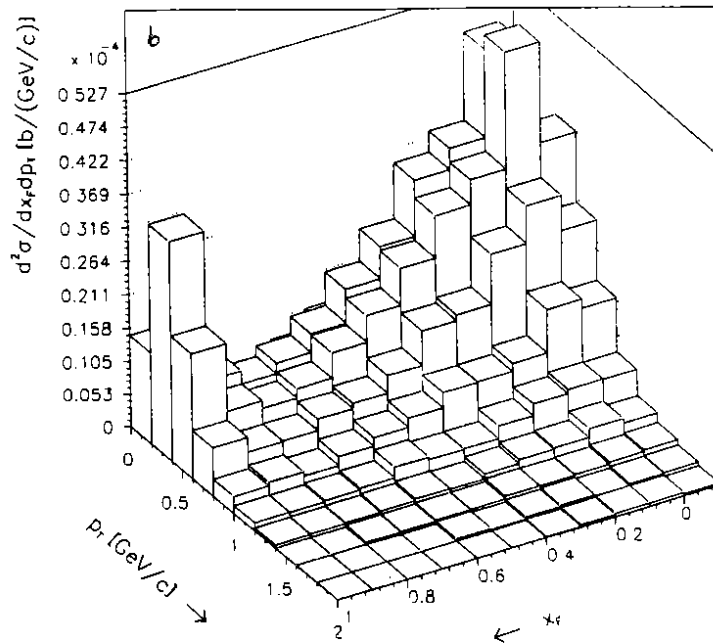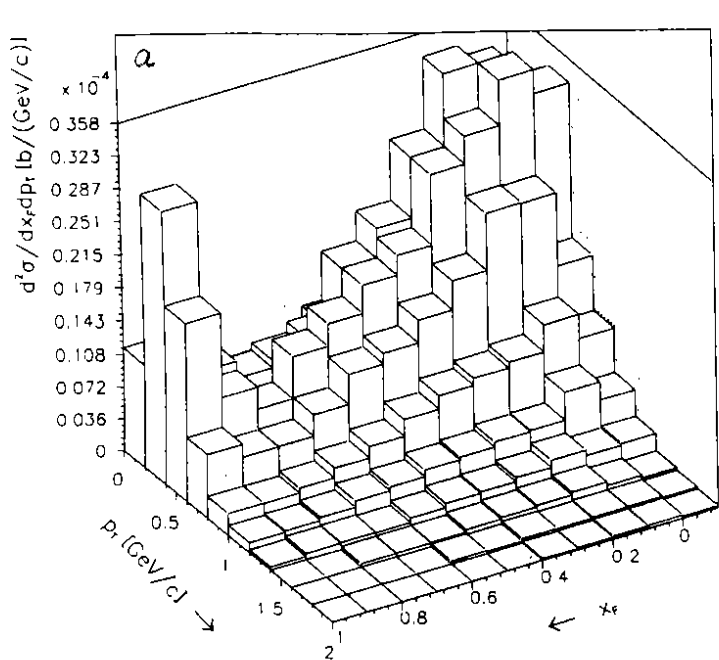The VMD model predicts that this ratio is about 1/200 [1] and in the simplest case constant everywhere.

12

Figure 5: Double differential cross sections, (a) γp data of low energy,
(b) γp data of high energy, (c) hp data of low energy, (d) hp data of high energy
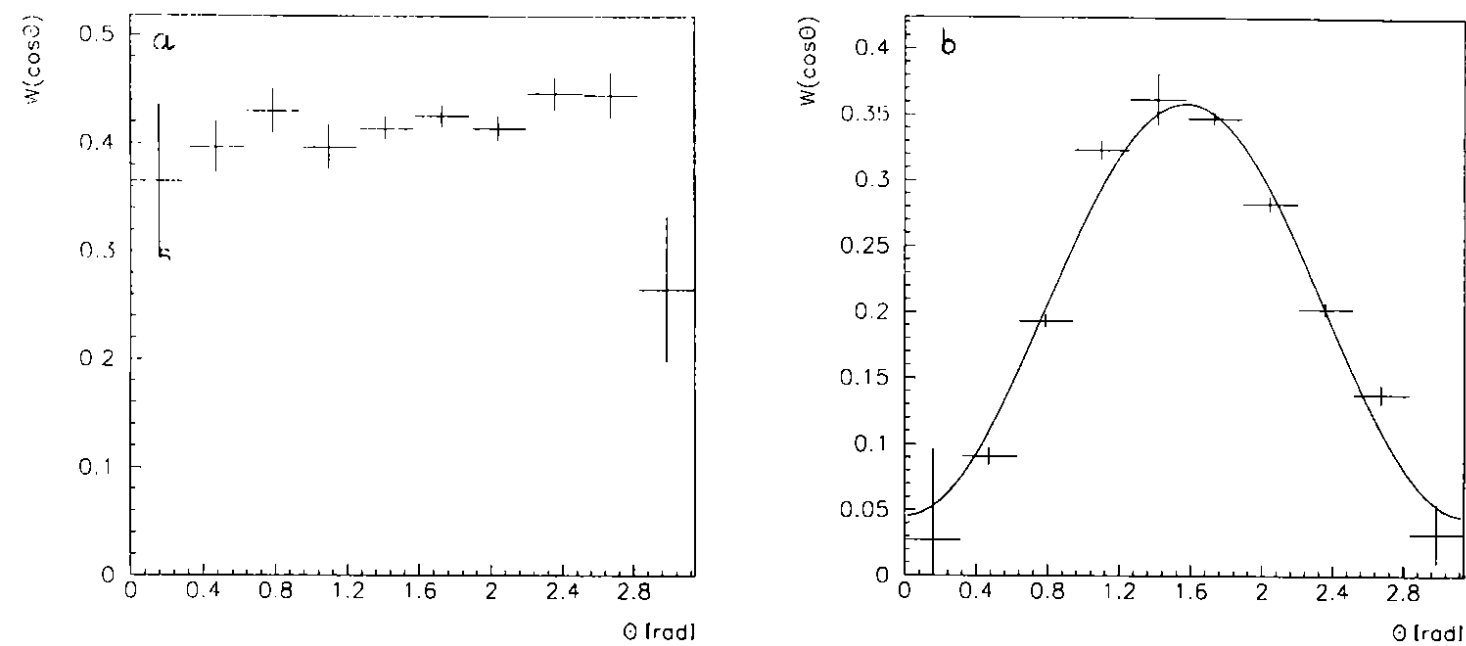
Figure 6: Polar decay angular distribution of the ρ^0 for γp data of $p_T \leq 0.6$ GeV/c
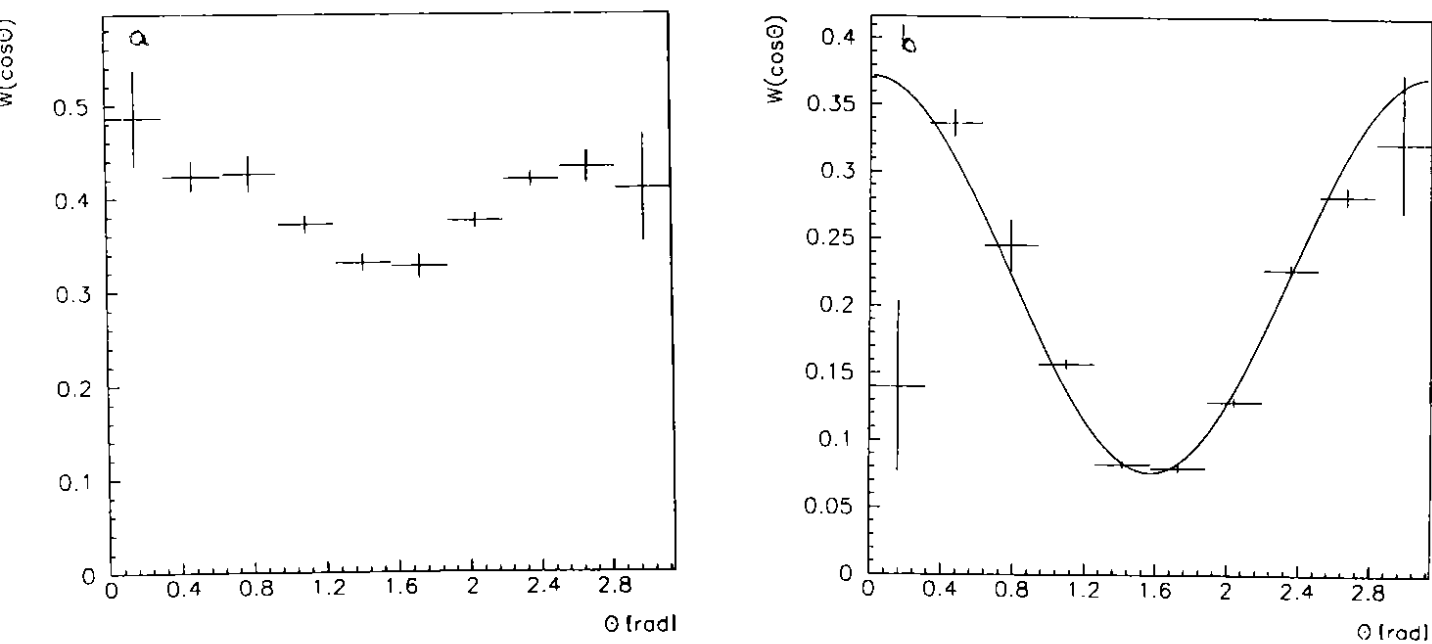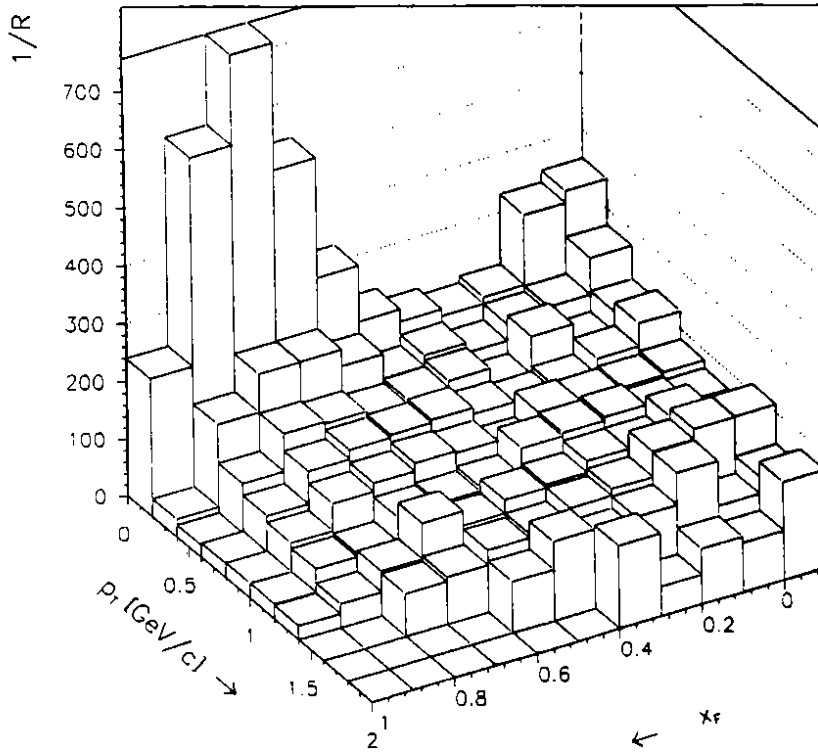and (a) $-0.1 \leq x_F \leq 0.5$, (b) $x_F \geq 0.8$. The curve is explained in the text.

Figure 7: Polar decay angular distribution of the ρ^0 for hp data, $p_T \leq 0.6$ GeV/c and (a)
$-0.1 \leq x_F \leq 0.5$, (b) $x_F \geq 0.8$. The curve is explained in the text.

14

Figure 8: $\sigma_{hadron}/\sigma_{photon}$, all energies

Considering figs. 5 and 8 three regions can be distinguished with respect to x_F and p_T of ρ^0:

1. The "triple-regge region" at large x_F ($x_F \geq 0.8$) with enhanced cross sections for both γp and hp data.

2. The "central production region" ($-0.1 \leq x_F \leq 0.7$ and $p_T \leq 1.6$ GeV/c) with an approximately flat area except for $p_T \leq 0.2$ GeV/c, i. e. excluding lowest and high p_T. In this region the ratio varies by less than 30% and the following values were calculated from the cross sections in the kinematical range considered:

$$R_L = 1/(197.4 \pm 3.3) \text{ at low energy and}$$

$$R_H = 1/(205.8 \pm 3.5) \text{ at high energy.}$$

These numbers agree with a corresponding analysis on inclusive production of charged particles by this experiment where R=1/(215±30) was measured [2].

3. The "high p_T" region with a nearly constant ratio at low x_F and a smooth decrease with increasing p_T at large x_F indicating an excess of the γp data. Such an excess was already detected in the inclusive charged particle study [2].

The details of the different regions will be discussed in the sections 5.3 to 5.5.

5.3 Production at large x_F

The cross section enhancement in the photon data set at high x_F ($x_F \geq 0.8$) (see figs. 5a, b) becomes even more evident in the projection onto the x_F axis, presented in lorentz invariant form in fig. 10. It is known [21] that forward photoproduction of ρ^0-mesons can be quantified in terms of a triple regge exchange mechanism. The underlying diagram is sketched in fig. 11a. In the limit $x_F \to 1$ the cross section can be written as

$$\frac{d^2\sigma(\gamma p \to \rho^0 X)}{dt d(M^2/s)} = \frac{1}{16\pi} \left(\frac{s}{M^2}\right)^{2\alpha_P(t)-1} \beta_{ppP}(0)\beta^2_{\gamma\rho P}(t)G_{PPP} \, . \tag{7}$$
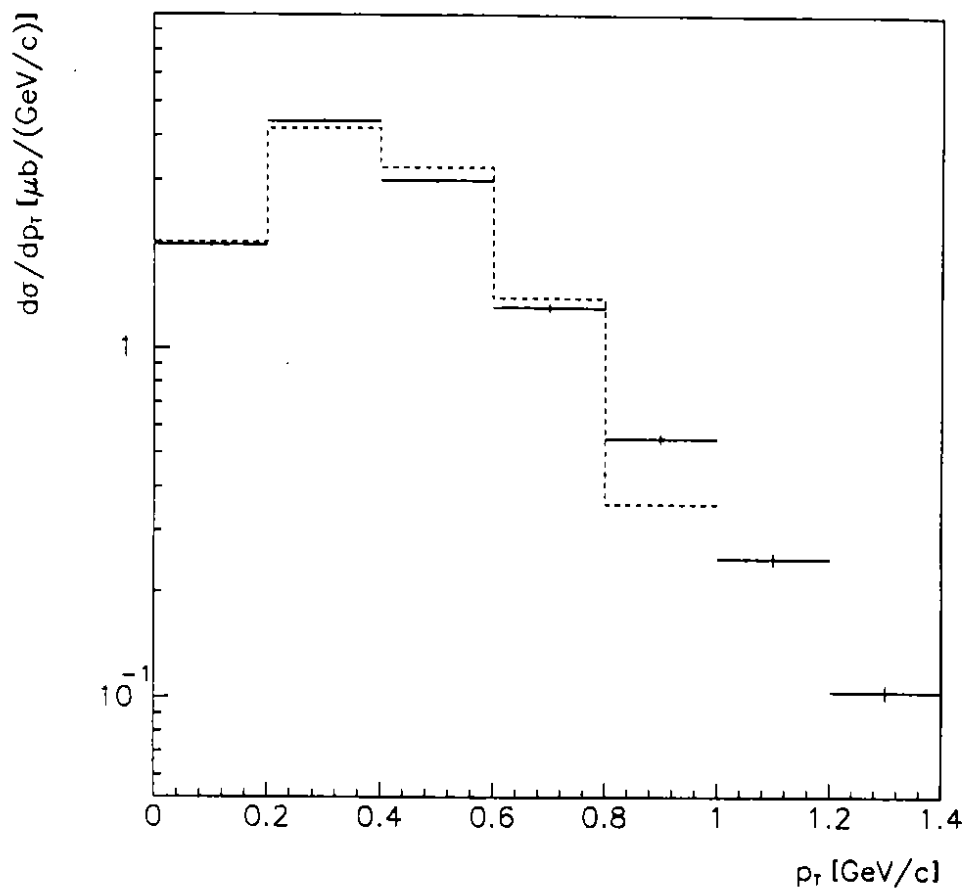
15

Figure 9: Diffractive dissociation cross section $d\sigma/dp_T$, $x_F(\rho^0) \geq 0.8$, γp data, all energies; the dashed line is explained in the text
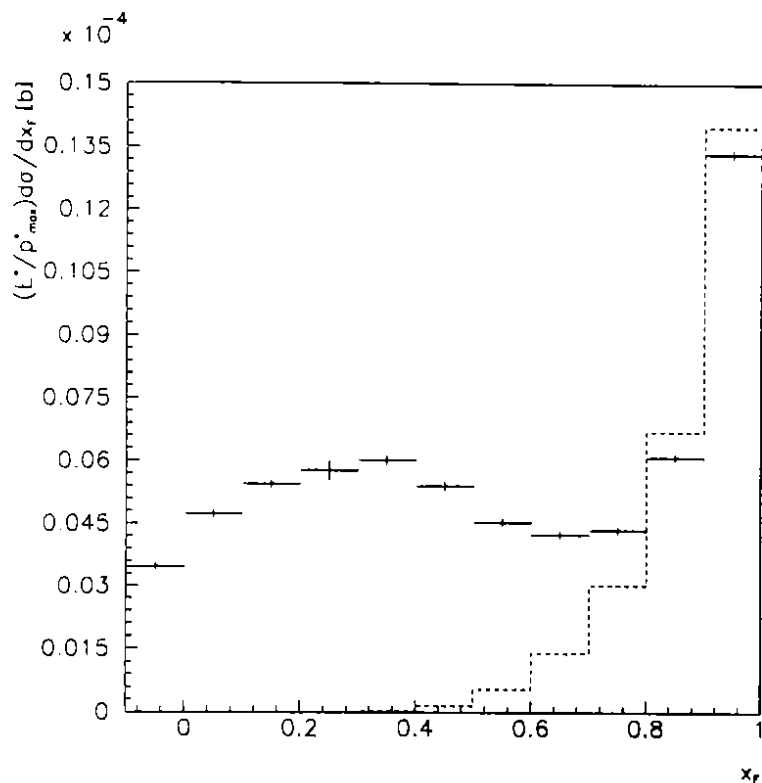

Figure 10: $(E/p^*_{max}) \cdot d\sigma/dx_F$, γp data, all energies; the dashed line indicates a triple regge prediction (see text)
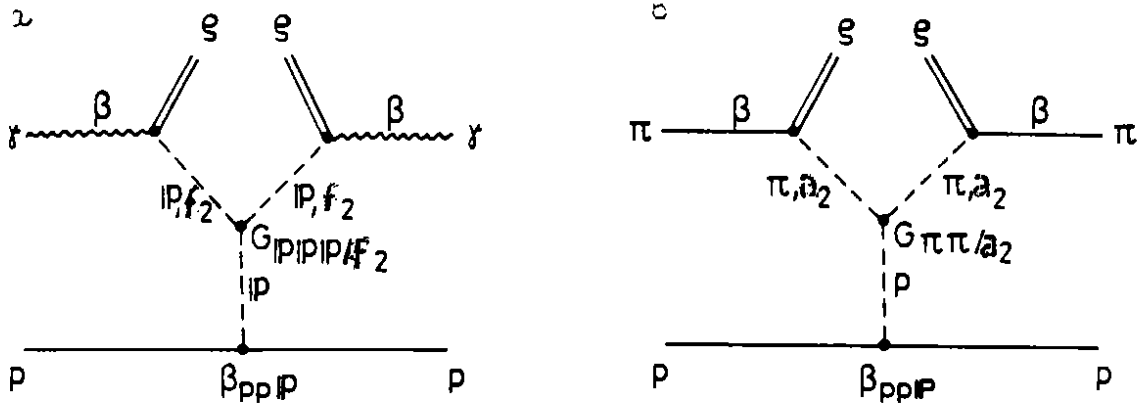
16

Figure 11: The triple regge exchange mechanisms

$$
\cdot \left\{ 1 + 2C \left(\frac{s}{M^2} \right)^{\alpha(t)} \cos \left(\frac{\pi}{2} \alpha(t) \right) + C^2 \left(\frac{s}{M^2} \right)^{2\alpha(t)} \right\}
$$

where the proton proton pomeron vertex form factor β_{ppP} and the triple regge coupling G_{PPP} are taken as in [3, 22], respectively. M denotes the invariant mass of X, s, t are the usual Mandelstam variables and C is a constant. $\alpha_P(t) = 1.086 + 0.25t$ is the pomeron trajectory, $\alpha(t) = -0.64 + 0.68t$ is the difference between the f_2 and the pomeron trajectory. The photon ρ^0 pomeron vertex form factor $\beta^2_{\gamma\rho P}(t)$ was deduced from the measurement of elastic ρ^0 production according to [3]:

$$
\beta^2_{\gamma\rho P}(t) = 16\pi \cdot \frac{d\sigma}{dt}(\gamma p \rightarrow \rho^0 p) \cdot \beta^{-2}_{ppP}.
\tag{8}
$$

The term in curly brackets corresponds to contributions from pomeron and f_2 exchange added coherently due to equal P and C quantum numbers. Their relative weight and the absolute normalisation were evaluated by fitting $d\sigma/dp_T(x_F(\rho^0) \geq 0.8)$ as shown in fig. 9.

The hence deduced quantitative prediction is shown in fig. 10 after integration over t.

The preponderant description of ρ^0 production at large x_F and low p_T in terms of the triple pomeron mechanism receives further support from the observation of a dominant $\sin^2 \theta$ shape of the ρ^0 decay angular distribution in the s-channel helicity system (see fig. 6) which is a well-known prediction for diffractive vector meson production with photons.

In the hp data a similar peak in the ρ^0 cross section at large x_F and somewhat lower p_T than in the photon data emerges. It is an effect associated exclusively with the pion beam data, and is independent of the beam energy (see tables 3,4) and of the charge of the incident pion. It has a steeper p_T distribution than the photo-induced data. The ρ^0 polar decay angular distribution in the s-channel helicity system (fig. 7) is consistent with the shape $W(\cos \theta) \propto (a + \cos^2 \theta)$ with $a = 0.254 \pm 0.011$ (see sec. 4). This angular dependence is what is expected from pion exchange [23], and the triple regge diagram of fig. 11b is a natural interpretation. The x_F- p_T dependence of the cross section can be
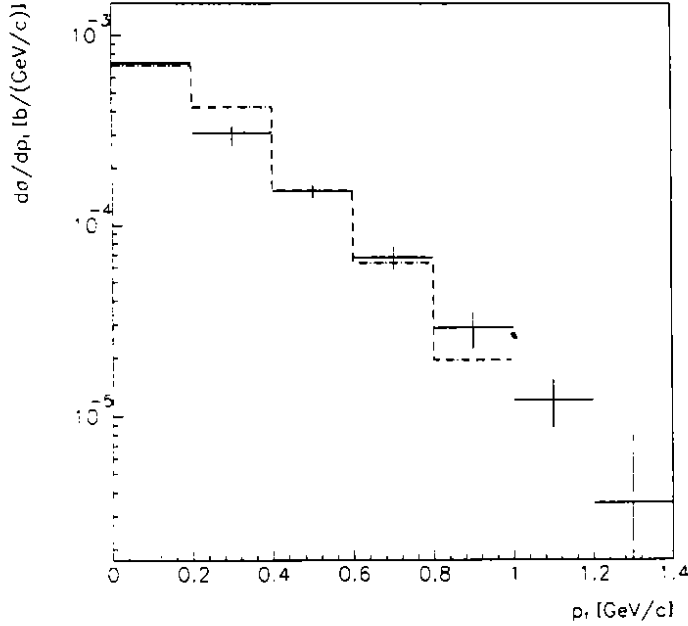
17

Figure 12: Triple regge cross section $d\sigma/dp_T, x_F(\rho^0) \geq 0.8$, πp data, all energies

explained by an analogue to eq. (7)

$$\frac{d^2\sigma(\pi p \to \rho^0 X)}{dt\,d(M^2/s)} \propto \left(\frac{s}{M^2}\right)^{2\alpha_\pi(t)-1} G_{\pi\pi P}(t) + \left(\frac{s}{M^2}\right)^{2\alpha_{a_2}(t)-1} G_{a_2 a_2 P}(t) \qquad (9)$$

where

$$G_{\pi\pi P}(t) \propto \frac{\exp(6t)}{(t-m_\pi^2)^2}$$

and

$$G_{a_2 a_2 P}(t) = \text{constant}$$

including a part from a_2 exchange responsible for the flattening of the p_T distribution for higher p_T. The overall normalisation and the relative weights are fixed again by fitting eq. (9) to the measured values of $d\sigma/dp_T$ (fig. 12), the corresponding x_F distribution is shown in fig. 13.

5.4 Production at low x_F and low p_T

In the non-diffractive or central kinematical domain it is assumed that photo- and hadro-production can be described in terms of the "quark-antiquark fusion" model. Inspired by the Drell-Yan mechanism this model is based on the assumption that the meson is produced by picking up one quark or antiquark from the beam (sea or valence quark) the other one from the target. The resulting invariant cross section ($\frac{2E^*}{\sqrt{s}} \cdot \frac{d\sigma}{dx_F}$) is then simply determined by a convolution of the structure functions involved, where all contributions ($S_{\gamma/h} * S_p, S_{\gamma/h} * V_p, V_{\gamma/h} * S_p, V_{\gamma/h} * V_p$) are taken into account. S indicates the sea quark, V the valence quark distributions of beam and target particles.

The $q\bar{q}$ fusion ansatz was applied to the data in the range $-0.1 \leq x_F \leq 0.7$ of the ρ^0. In all cases the proton structure function as given by [24] was included. This structure function is known to fit the EMC-data [25] at low Q^2. For the γp data the photon structure function recently determined in the TPC experiment at $Q^2 \approx 0.7 (\text{GeV}/c)^2$ [26] was used first. The comparison to WA69 data is shown in fig. 12a (full line), where the triple regge part has been subtracted.
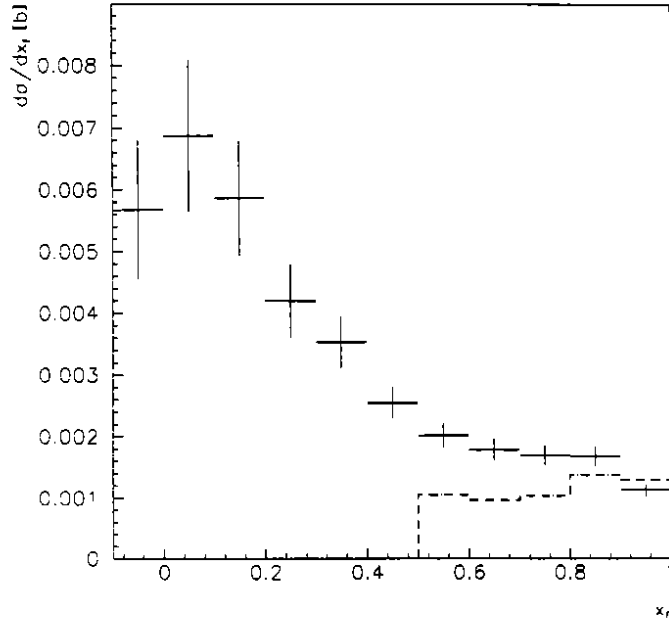
18

Figure 13: $d\sigma/dx_F$, πp data, all energies

The πp data in fig. 14b were compared to the same structure function (full line). The dotted line shows the result of the triple regge calculation (fig. 13).

The Kp data were used to fit valence and sea quark structure functions of the kaon according to

$$x v_K(x) = x^{0.5} \cdot (1 - x)^{(1.75 \pm 0.10)} \cdot B^{-1}(0.5, (1.75 \pm 0.10) + 1)$$

$$x s_K(x) = (0.03 \pm 0.01) \cdot (1 - x)^{(9.0 \pm 2.0)}$$

where B is the β-function assuring the normalisation of the valence quark structure function. The dashed curve in fig. 14c shows this fit result. The difference between the data and the curve is caused by remnants of K* or by production mechanisms analogous to fig. 11. The photon structure functions were determined with an identical ansatz fitted simultaneously to the kaon and photon data. The fit yielded for the photon

$$x v_\gamma(x) = x^{0.5} \cdot (1 - x)^{(1.4 \pm 0.2)} \cdot B^{-1}(0.5, (1.4 \pm 0.2) + 1)$$

$$x s_\gamma(x) = (0.025 \pm 0.010) \cdot (1 - x)^{(1.0 \pm 0.3)}$$

(dashed line in fig. 14a). The general trend of these results is similar to that found in [26].

Assuming the pion structure functions being equal to the photon structure functions, the results for the photon were used to predict the πp cross sections (dashed curve in fig. 14b).

The quark content of the ρ^0 inhibits sensitivity to either the strange quark content of the beam or the strangeness sea suppression factor. This is not the case for the inclusive production of ϕ and K*. A corresponding analysis is in preparation.

5.5 High p_T Production

In fig. 15 the ratio of cross sections between $\gamma p \to \rho^0$ X and hp $\to \rho^0$ X is shown as a function of p_T. The distribution corresponds to the p_T projection of fig. 8 where $x_F \geq 0.8$ has been excluded.
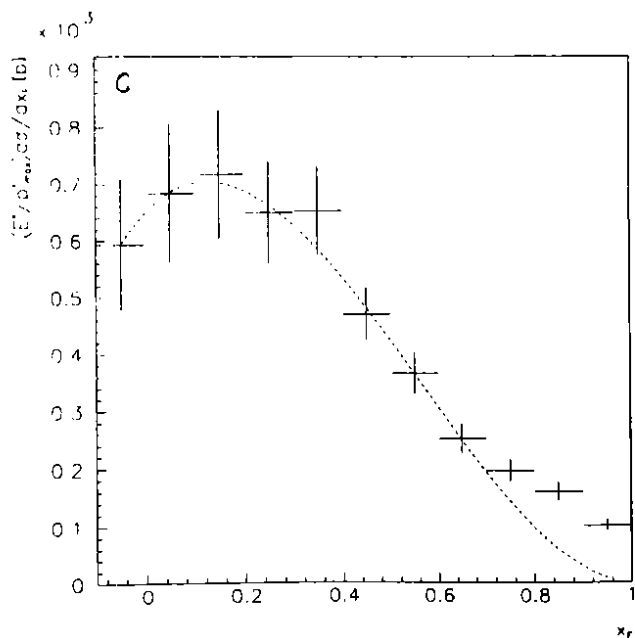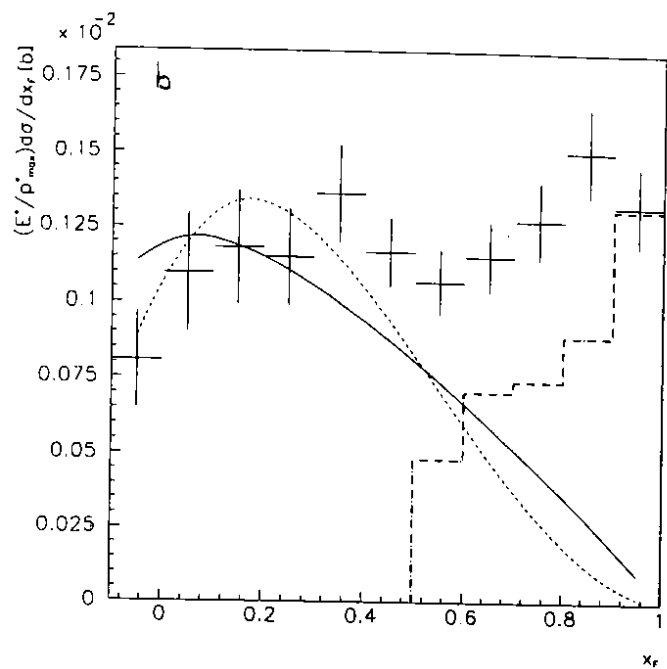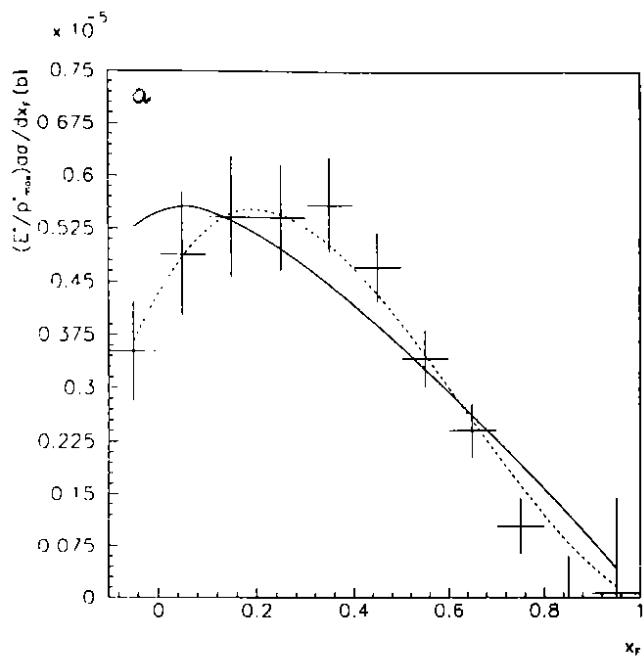
Figure 14: Lorentz invariant cross sections, (a) γp data of high energy (triple regge part has been subtracted), (b) πp data of high energy, (c) Kp data of high energy
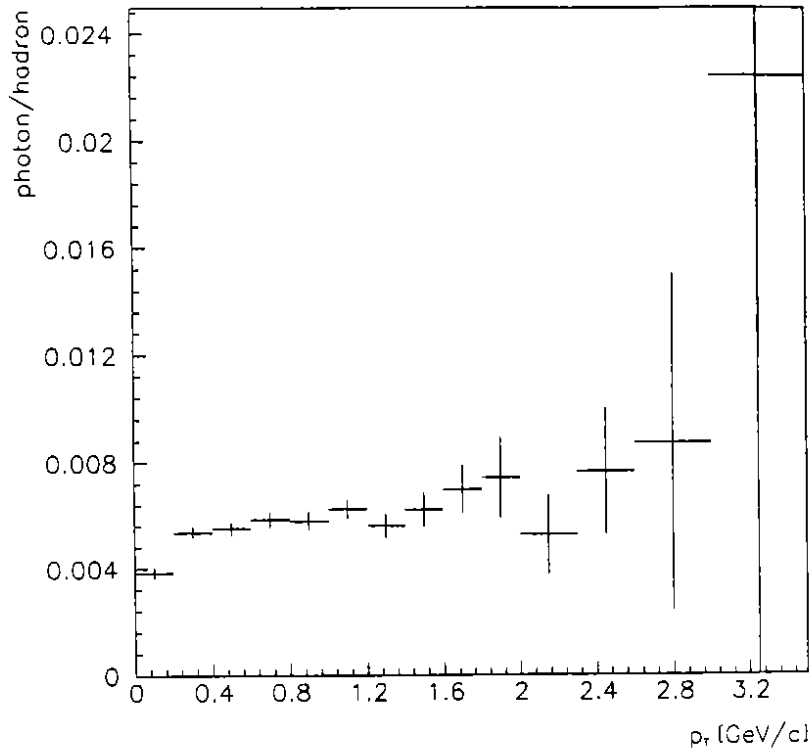
Figure 15: VMD factor as a function of p_T for high energy data

At low p_T the ratio is constant for p_T values up to about 1.6 GeV/c and its magnitude represents the VMD factor discussed in section 5.1.

Above 1.6 GeV/c the ratio grows with p_T according to an extra contribution of pointlike photon interactions already observed in p_T distributions of inclusive pions [2], [27], [4] and azimuthal energy flows [5]. In the region with $p_T \geq 1.6$ GeV/c, the high energy data yield a ratio $R_H = 1/(146 \pm 14)$ compared to $R_H = 1/(205.8 \pm 3.5)$ at $p_T \leq 1.6$ GeV/c (see section 5.2).

The excess of the γp data at high p_T ρ^0 production is well described by the LUND Monte Carlo program LUCIFER [9]. This is shown in fig. 16 where $(d\sigma/dp_T)(\gamma p \to \rho^0 X)$ is compared to the sum of $1/VMD \cdot (d\sigma/dp_T)(hp \to \rho^0 X)$ and the LUCIFER predicted p_T dependent cross sections.

6   SUMMARY AND CONCLUSIONS

This paper reports on the inclusive measurement of $\rho^0(770)$ mesons with photon and hadron beams as a function of x_F and p_T in the energy range from 65 GeV $\leq E \leq$ 175 GeV. A key element for this purpose was the use of identical detector setup, trigger and software for either data. We observe a ρ^0 line shape which is not well described by a pure Breit-Wigner function throughout most of the x_F- p_T plane but can be fitted by allowing in addition an interference between the ρ^0 amplitude and nonresonant pion pair production. This interference is needed for both, photon and hadron beam data but is more pronounced in the photon case.

The ratio of the cross sections R $= \sigma(\gamma p \to \rho^0 X)/\sigma(hp \to \rho^0 X)$ integrated over x_F and p_T yields R $= 1/(197.4\pm3.3)$ at low energy and R $= 1/(205.8\pm3.5)$ at high energy in accordance with expectations from vector meson dominance. R is measured as a function of x_F and p_T. At low p_T and large x_F ρ^0 production is well quantified within the framework of triple regge exchange pictures with pomeron, f_2 for photon and π, a_2 for hadron induced data, respectively. Excluding large x_F phenomena both data sets are dominated by soft
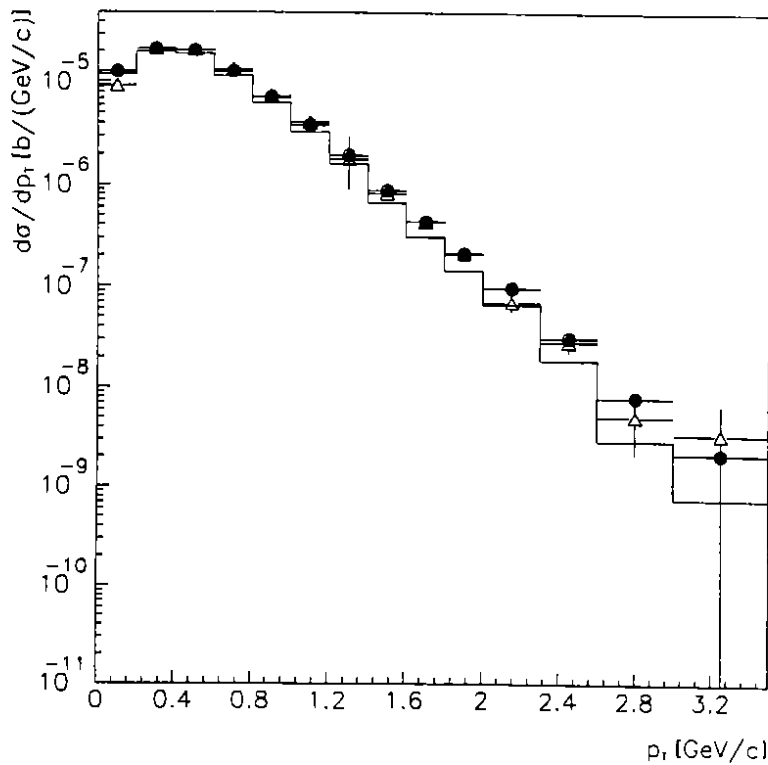
Figure 16: Comparison of photon cross sections(triangles) to 1/200·hadron(histogram) and (1/200·hadron + LUCIFER)(full circles) for high energy data

processes which are consistent with ρ^0 production in a quark (from target) quark (from beam) fusion picture.

At $p_T \geq 2.0$ GeV ρ^0 photoproduction shows a significant onset due to pointlike mechanisms.

Aknowledgements

REFERENCES

[1] D.W.G.S. Leith, Electromagnetic Interaction of Hadrons, ed. Donnachie and Shaw, Vol. I, Plenum Press N. Y. 1978, 345

[2] R.J. Apsimon et al., Z. Phys. C43 (1989) 63

[3] M. Atkinson et al., Nucl. Phys. B245 (1984) 189

[4] E. Auge et al., Phys. Lett. 168B (1986) 163
    R. Barate et al., Phys. Lett. 174B (1986) 458

[5] R.J. Apsimon et al., Z. Phys. C46 (1990) 35

[6] A. O'Connor, OMFATHAC User's Guide, Lancaster (1988), unpublished "

[7] J.C. Lassalle et al., CERN-DD/EE/79-2, and NIM 176 (1980) 371

[8] G. Marchesini, B.R. Webber, CERN Pool Program W5037 (1989)

[9] H.U. Bengtsson, G. Ingelman, T. Sjöstrand, A. Weigend, CERN Pool Program W5035/W5045...W5048(1987)

[10] Particle Data Group, Phys. Lett. B204 (1988)

[11] J.L. Bailly et al., Z. Phys. C36 (1987) 545

[12] L.J. Lanzeroti et al., Phys. Rev. Letters 15 (1965) 210

[13] P. Söding, Phys. Lett. 19 (1966) 702

[14] G. Kramer, H.R. Quinn, Nucl. Phys. B27 (1971) 77

[15] K. Abe et al., Phys. Rev. D32 (1985) 2288

[16] M. Schouten et al., Z. Phys. C9 (1981) 93

[17] N.M. Agababyan et al., Z. Phys. C46 (1990) 387

[18] M. Aguilar-Benitez et al., Z. Phys. C44 (1989) 531

[19] M. Barth et al., Nucl. Phys. B223 (1983) 296

[20] N.M. Agababyan et al., Z. Phys. C41 (1989) 539

[21] P.D.B. Collins, A.D. Martin, Rep. Prog. Phys. 45 (1982) 335

[22] A. Donnachie, P. Landshoff, Nucl. Phys. B231 (1984) 189

[23] J.A. Poirier et al., Ph. Rev. 136 (1967) 1462

[24] A. Donnachie, P. Landshoff, Nucl. Phys. B244 (1984) 322

[25] M. Arneodo et al., Nucl. Phys. B333 (1990) 1

[26] H. Aihara et al., Z. Phys. C34 (1987) 13

[27] R.J. Apsimon et al., to be published